ORIGINS OF HYDRODYNAMIC FORCES ON CENTRIFUGAL PUMP IMPELLERS

Douglas R. Adkins* and Christopher E. Brennen
California Institute of Technology
Pasadena, California 91125

Hydrodynamic interactions that occur between a centrifugal pump impeller and a volute are experimentally and theoretically investigated. The theoretical analysis considers the inability of the blades to perfectly guide the flow through the impeller, and also includes a quasi-one dimensional treatment of the flow in the volute. The disturbance at the impeller discharge and the resulting forces are determined by the theoretical model. The model is then extended to obtain the hydrodynamic force perturbations that are caused by the impeller whirling eccentrically in the volute. Under many operating conditions, these force perturbations were found to be destablizing. Comparisons are made between the theoretical model and the experimental measurements of pressure distributions and radial forces on the impeller. The theoretical model yields fairly accurate predictions of the radial forces caused by the flow through the impeller. However, it was found that the pressure acting on the front shroud of the impeller has a substantial effect on the destablizing hydrodynamic forces.

NOMENCLATURE

b	width of impeller discharge
h	total head $(h^* = 2h/\rho\Omega^2 R_2^2)$
j	$\sqrt{-1}$
$\underset{\sim}{k}$	impeller phase coefficient = $\cos(\tan\gamma \ln(R)) + j\sin(\tan\gamma \ln(R))$
r,θ	polar coordinate system
s	length in tangential direction
t	time
v	relative velocity in impeller
w	width in volute
x,y,z	rectangular coordinate system

---

* Now at Sandia National Laboratories, Albuquerque, NM 87185

$\overline{A},\overline{rA},\overline{rrA}$ $\overline{\ln rA},\overline{r\ln rA}$	moments of volute cross-sectional area (defined in Equations 14a-e)
A_{ij}	$(i = x,y\ ,\ j = x,y)$ components of generalized hydrodynamic force matrix [A] $(A^*_{ij} = A_{ij}/\rho\pi b\Omega^2R_2^3)$
C_{ij}	$(i = x,y\ ,\ j = x,y)$ components of damping force matrix [C] $(C^*_{ij} = C_{ij}/\rho\pi b\Omega R_2^2)$
D_p	pressure coefficient at volute inlet = $2(P_v(R_2',\theta') - h_1)/\rho\Omega^2R_2^2$
F	force acting on impeller $(F^* = F/\rho\pi b\Omega^2R_2^3)$
$F(t)$	integration constant in Bernoulli's equation
J_{ij}	$(i = x,y\ ,\ j = x,y)$ coefficients of the jerk force matrix [J] $(J^*_{ij} = J_{ij}/\rho\pi bR_2^2/\Omega)$
K_{ij}	$(i = x,y\ ,\ j = x,y)$ components of stiffness force matrix [K] $(K^*_{ij} = K_{ij}/\rho\pi b\Omega^2R_2^2)$
M_{ij}	$(i = x,y\ ,\ j = x,y)$ components of inertia force matrix [M] $(M^*_{ij} = M_{ij}/\rho\pi bR_2^2)$
P_i	pressure in impeller $(P_i^* = 2P_i/\rho\Omega^2R_2^2)$
P_v	pressure in volute $(P_v^* = 2P_v/\rho\Omega^2R_2^2)$
R	impeller radius (with no subscript, $R = R_2/R_1$)
R_t	radius of pressure tap ring
V	velocity in volute (with no subscript, $V^* = V_{\theta'}/\Omega R_2$)
W_i	width of impeller at R_2 $(W_i^* = W_i/b)$
β	perturbation function for impeller flow
ζ	angular location of the impeller center $(= \omega t = \text{constant})$
γ	angle of flow path through impeller
ε	distance between impeller and volute centers $(\varepsilon^* = \varepsilon/R_2)$
ρ	fluid density
ϕ	flow coefficient = flowrate through pump/$2\pi b\Omega R_2^2$
ψ	total head rise coefficient = $(ha - h_1)/\rho\,\Omega^2R_2^2$
ω	orbit speed of impeller center (whirl speed)

Ω	rotational speed of impeller (shaft speed)

Subscripts:

c,s	cos ωt and sin ωt components (non-dimensionalized)
d	downstream of pump
exp	experimental result
m	force component due to momentum exchange
p	force component due to pressure
r,θ	radial or angular component
x,y	components in rectangular directions (real = x and imaginary = y)
1,2	impeller inlet and discharge

Superscripts:

'	measurement made in volute reference frame
''	measurement made from frame fixed to rotating impeller
*	non-dimensionalized quantity

Special Notation:

$\underset{\sim}{v}$	underbar denotes vector quantity
$\bar{V}$	overbar denotes centered impeller value (non-dimensionalized)
[A]	square brackets denote a matrix quantity
$\dot{x}$	dot represents a time derivative

INTRODUCTION

Several sources, both dynamic and hydrodynamic have been identified as contributing to the forces on centrifugal pump impellers. Figure 1 shows a typical configuration for a centrifugal pump with a few of the key components identified. The primary emphasis of this study was to investigate the forces that result from the hydrodynamic interaction between the impeller and the volute. The usual design criterion for a volute is that it should provide minimum interference to the symmetric impeller discharge flow that would occur if no volute was present. However, the discharge flow pattern will depend upon the overall flowrate through the impeller. Once the flowrate changes, the discharge conditions around the impeller become asymmetric for any given volute. Even at the volute design flowrate, the discharge conditions could still become asymmetric if the impeller is displaced from the "design" center of the volute by shaft deflection, bearing wear, etc.. In either case, the end result of the asymmetric discharge conditions is that there will be a net radial force on the impeller (see Figure 1).

It is customary in rotordynamic analyses to linearize the radial forces acting on the rotor in terms of a steady portion acting on the centered impeller, and a time dependent part due to the impeller whirling in a small circular orbit. Referring to Figure 1, these terms may be expressed as

$$\begin{Bmatrix} F_x^* \\ F_y^* \end{Bmatrix} = \begin{Bmatrix} \bar{F}_x \\ \bar{F}_y \end{Bmatrix} + \begin{bmatrix} A_{xx}^* & A_{xy}^* \\ A_{yx}^* & A_{yy}^* \end{bmatrix} \begin{Bmatrix} \varepsilon^* \cos \omega t \\ \varepsilon^* \sin \omega t \end{Bmatrix} \tag{1}$$

where $\bar{F}_x$ and $\bar{F}_y$ result from the interaction of the centered impeller with the volute, and the matrix [A] relates the perturbed force to the eccentric position of the impeller. The [A] matrix will be a function of the whirl speed, ω, and is often expressed as a quadratic in ω so that the system resembles a simple stiffness, damping, and mass model.

The steady or mean forces, $\bar{F}_x$ and $\bar{F}_y$, have been examined in several studies and an understanding of them has been greatly enhanced through papers by Iversen et al. [9], Csanady [7], and Agostinelli et al. [2] to name a few. All of these authors have shown that there is a particular flowrate where forces on the impeller will be minimized for a given volute. Previous experimental [5,10] and theoretical [6] investigations have also shown that the components of [A] are such that a whirling motion of the impeller would be encouraged rather than dissipated by the hydrodynamic effects. This has created concern that the rotor assembly may whirl at one of its critical speeds even though the shaft may be rotating well above this speed. There also exists the problem of the alternating flexural stress that would be developed if the impeller whirls at a subsynchronous speed (see Ehrich and Childs [8]).

In the current study, a theoretical model of the volute and impeller flows will be developed and compared to experimental results. Previously, a potential flow model for the steady forces on a centered impeller was given by [7] and this work was later extended by [6] to include the effects of the impeller whirling within the volute. Although the potential flow model presents a more classical approach of solving for the forces, problems arise in relating the two dimensional theoretical volute profile to the three dimensional geometry of a real volute. For this reason, a bulk flow description of the flow through the volute is chosen for the current work. A similiar treatment of the volute flow was presented by [9], but the influence of this flow on the impeller discharge conditions was largly ignored and only the non-whirling impeller was considered. The impeller/volute interaction will be included along with the effects of impeller whirl in the present analysis.

THEORETICAL ANALYSIS

In developing the theoretical model, the problem is broken into its two natural parts; models are constructed for the flow through the impeller and in the volute. The equations that are generated in these two parts are then combined by matching the pressures and velocities at the impeller discharge to those at the volute inlet. A full development of this model can be found in reference [1] and only brief summary will be presented here.

Governing Equations for the Impeller

Figure 2 illustrates the geometries used in developing the impeller model. To relate the pressure between the inlet and discharge of the impeller, a simplified unsteady form of Bernoulli's Equation is written as

$$\frac{P_i}{\rho} + \frac{v^2}{2} - \frac{\Omega^2 r''^2}{2} + \int_{s''} \frac{\partial v}{\partial t}\, ds'' - \omega^2 \varepsilon \int_{s''} \cos(\omega t - \Omega t - \theta'')\, dr'' - \omega^2 \varepsilon \int_{s''} \sin(\omega t - \Omega t - \theta'')\, r'' d\theta'' = F(t) \qquad (2)$$

Here the flow is assumed to be two dimensional and the impeller whirl speed constant.

To simplify the model, certain assumptions must be made about the velocity field within the impeller. Specifically, the flow in the impeller is assumed to follow a spiral path with inclination angle, γ, which is fixed relative to the impeller for a given flowrate and head rise so that

$$\theta_2'' = \theta'' + \tan\gamma \ln(r''/R_2) \qquad (3)$$

Here (r'', θ'') and (R_2, θ_2'') are the coordinates of a general point on a streamline within the impeller and at the position of discharge respectively. The flow path angle, γ, of the streamlines is permitted to deviate from the impeller blade angle. It is determined in a manner described in Section 2(c) so that the theoretical and experimental head/flowrate characteristics coincide. To account for the asymmetry caused by the volute, a circumferential perturbation is superimposed on this impeller flow. This flow perturbation is assumed to be stationary in the volute reference frame. Together, these observations require that

$$v = (v_{r''}^2 + v_{\theta''}^2)^{1/2} = \phi\, \Omega R_2^2\, \beta(\theta'', r'', \Omega t, \omega t, \varepsilon) \sec\gamma / r'' \qquad (4)$$

The perturbation function β, must from continuity considerations be constant along a streamline. For whirl motions with small eccentric orbits, β may be linearized as

$$\beta(\theta'', r'', \Omega t, \omega t, \varepsilon) = \bar{\beta}(\theta_2) + \varepsilon^* \{\beta_c(\theta_2) \cos\omega t + \beta_s(\theta_2) \sin\omega t\} \qquad (5)$$

Equations (4) and (5) can now be substituted into Equation (2). The pressure at the impeller discharge is then given as a function of β and the inlet pressure. The pressure is not known at the inlet of the impeller, but it can be written in terms of the inlet total head which is assumed to be circumferentially constant. If there is no pre-swirl at the inlet, this will give the inlet pressure as

$$P_i^*(R_1,\theta_1) \cong h_1^* - \phi R \bar{\beta}(\theta_2)\{\phi R \bar{\beta}(\theta_2) + 2\varepsilon^* \frac{\omega}{\Omega}\sin(\theta_1 - \omega t)\}$$
$$- 2\varepsilon^* \phi^2 R^2 \bar{\beta}(\theta_2)\{\beta_c(\theta_2)\cos\omega t + \beta_s(\theta_2)\sin\omega t\} \qquad (6)$$

for small eccentric displacements. By utilizing Equations (4) through (6) and neglecting terms of order ε^2 and higher, Bernoulli's Equation can now be separated into harmonics with steady, $\varepsilon\cos\omega t$, and $\varepsilon\sin\omega t$ dependence as

$$\phi \sec^2\gamma[2\ln(R)\frac{d\bar{\beta}}{d\theta_2} + \phi\bar{\beta}^2] + \bar{D}_p - 1 = 0 \qquad (7a)$$

$$2\phi\sec^2\gamma[\ln(R)\frac{d\beta_c}{d\theta_2} + \phi\bar{\beta}\beta_c + \frac{\omega}{\Omega}\ln(R)\beta_s] + D_{pc} - \sin\theta_2\frac{d\bar{D}_p}{d\theta_2}$$
$$+ 2\frac{\omega}{\Omega}[\phi R\bar{\beta}\sin(\theta_2 + \tan\gamma\ln(R)) - \cos(\theta_2 + \tan\gamma\ln(R))/R]$$
$$- 2\frac{\omega^2}{\Omega^2}[\cos\theta_2 - \cos(\theta_2 + \tan\gamma\ln(R))/R]/\tan^2\gamma = 0 \qquad (7b)$$

$$2\phi\sec^2\gamma[\ln(R)\frac{d\beta_s}{d\theta_2} + \phi\bar{\beta}\beta_s - \frac{\omega}{\Omega}\ln(R)\beta_c] + D_{ps} + \cos\theta_2\frac{d\bar{D}_p}{d\theta_2}$$
$$- 2\frac{\omega}{\Omega}[\phi R\bar{\beta}\cos(\theta_2 + \tan\gamma\ln(R)) + \sin(\theta_2 + \tan\gamma\ln(R))/R]$$
$$- 2\frac{\omega^2}{\Omega^2}[\sin\theta_2 - \sin(\theta_2 + \tan\gamma\ln(R))/R]/\tan^2\gamma = 0 \qquad (7c)$$

where

$$D_p(\theta') = \overline{D_p}(\theta') + \varepsilon^*[D_{pc}(\theta')\cos\omega t + D_{ps}(\theta')\sin\omega t] \qquad (8)$$

In Equations (7a-c) the impeller discharge pressure coefficient, $D_p(\theta')$, has been transformed into the impeller reference frame by the approximation, $\theta_2 = \theta' + \varepsilon^*\sin(\theta' - \omega t)$. This will prove convenient in the future, because the pressure at the impeller discharge is assumed to be equal to that at the volute inlet.

Governing Equations for the Volute

The geometries used in developing the volute model are shown in Figure 3. The volute flow will be described by a continuity equation, a moment of momentum equation, and an equation of motion in the radial direction. Each of these three equations can be written respectively as

$$\frac{\partial (wV_{\theta'})}{\partial \theta'} + \frac{\partial (wr'V_{r'})}{\partial r'} = 0 \tag{9}$$

$$\frac{\partial (wr'V_{\theta'}V_{\theta'})}{\partial \theta'} + \frac{\partial (wr'r'V_{\theta'}V_{r'})}{\partial r'} + wr'r'\frac{\partial V_{\theta'}}{\partial t} = -\frac{wr'}{\rho}\frac{\partial P_v}{\partial \theta'} \tag{10}$$

and

$$\frac{\partial P_v}{\partial r'} = \frac{\rho V_{\theta'}V_{\theta'}}{r'} \tag{11}$$

Here it has been estimated that $V_{r'}$, and $V_{z'}$ (and their gradients) are much less than $V_{\theta'}$, except at the inlet of the volute.

Within the volute, the flow is considered to be primarily in the θ′ direction and to have a flat velocity profile. This will allow Equations (9), (10), and (11) to be integrated over the volute cross-section. When these equations are combined with Equations (4) and (5), the pressure and velocity distributions in the volute will be given in terms of moments of the volute cross-sectional area and the perturbation function, β. Both Equations (9) and (10) can then be separated into three parts (steady, $\varepsilon \cos \omega t$, and $\varepsilon \sin \omega t$) as follows:

Continuity:

$$\frac{d(\overline{V}\,\overline{A})}{d\theta'} = \phi\overline{\beta} \tag{12a}$$

$$\frac{d(V_c\overline{A})}{d\theta'} = W_i^* \frac{d(\overline{V}\cos\theta')}{d\theta'} + \frac{\omega}{\Omega}\sin\theta' + \phi[\beta_c + \frac{d(\overline{\beta}\sin\theta')}{d\theta'}] \tag{12b}$$

$$\frac{d(V_s\overline{A})}{d\theta'} = W_i^* \frac{d(\overline{V}\sin\theta')}{d\theta'} - \frac{\omega}{\Omega}\cos\theta' + \phi[\beta_s - \frac{d(\overline{\beta}\cos\theta')}{d\theta'}] \tag{12c}$$

Moment of momentum:

$$\frac{\overline{rA}}{2}\frac{d\overline{D}_p}{d\theta'} = -\frac{d(\overline{rA}\,\overline{V}^2)}{d\theta'} - \overline{r\ln rA}\,\frac{d(\overline{V}^2)}{d\theta'} + \phi(1 - \phi\tan\gamma\,\overline{\beta})\overline{\beta} \tag{13a}$$

$$\begin{aligned}\frac{\overline{rA}}{2}\frac{dD_{pc}}{d\theta'} = &-2\frac{d(\overline{rA}\,\overline{V}\,V_c)}{d\theta'} + \frac{\omega}{\Omega}(W_i^*\sin\theta'\overline{V} - \overline{rrA}\,V_s)\\ &+ (W_i^* + \overline{rA})\frac{d(\overline{V}^2\cos\theta')}{d\theta'} - 2\overline{r\ln rA}\,\frac{d(\overline{V}\,V_c)}{d\theta'}\\ &+ \phi^2\sin\theta'\overline{\beta}^2 + \phi\cos\theta'\left(\frac{\omega}{\Omega} + 2 - 2\phi\tan\gamma\,\overline{\beta}\right)\overline{\beta}\\ &+ \phi(1 - 2\phi\tan\gamma\,\overline{\beta})\left(\beta_c + \sin\theta'\frac{d\overline{\beta}}{d\theta'}\right) + \frac{W_i^*}{2}\cos\theta'\frac{d\overline{D_p}}{d\theta'}\end{aligned} \tag{13b}$$

$$\begin{aligned}\frac{\overline{rA}}{2}\frac{dD_{ps}}{d\theta'} = &-2\frac{d(\overline{rA}\,\overline{V}\,V_s)}{d\theta'} - \frac{\omega}{\Omega}(W_i^*\cos\theta'\overline{V} - \overline{rrA}\,V_c)\\ &+ (W_i^* + \overline{rA})\frac{d(\overline{V}^2\sin\theta')}{d\theta'} - 2\overline{r\ln rA}\,\frac{d(\overline{V}\,V_s)}{d\theta'}\\ &- \phi^2\cos\theta'\overline{\beta}^2 + \phi\sin\theta'\left(\frac{\omega}{\Omega} + 2 - 2\phi\tan\gamma\,\overline{\beta}\right)\overline{\beta}\\ &+ \phi(1 - 2\phi\tan\gamma\,\overline{\beta})\left(\beta_s - \cos\theta'\frac{d\overline{\beta}}{d\theta'}\right) + \frac{W_i^*}{2}\sin\theta'\frac{d\overline{D_p}}{d\theta'}\end{aligned} \tag{13c}$$

where

$$\overline{A}(\theta') = \int_{R_2}^{R_3'} w\,dr'/bR_2\ ,\quad \overline{\ln rA}(\theta') = \int_{R_2}^{R_3'} \ln(r'/R_2)\,w\,dr'/bR_2$$

$$\overline{rA}(\theta') = \int_{R_2}^{R_3'} r'w\,dr'/bR_2^2\ ,\quad \overline{rrA}(\theta') = \int_{R_2}^{R_3'} r'r'w\,dr'/bR_2^3$$

$$\overline{r\ln rA}(\theta') = \int_{R_2}^{R_3'} r'\ln(r'/R_2)\,w\,dr'/bR_2^2 \tag{14a-e}$$

and

$$V^*(\theta') = \overline{V}(\theta') + \varepsilon^*[V_c(\theta')\cos\omega t + V_s(\theta')\sin\omega t] \cong \frac{V_\theta'}{\Omega R_2} \tag{15}$$

In Equations (12a-c) and (13a-c) the perturbation function, β, has been transformed into the volute reference frame for convenience in obtaining a solution.

To complete the basic equations for the volute problem, Equation (11) may be integrated to give the radial pressure variation in the volute as

$$P_v^* = \overline{D_p} + 2\bar{V}^2[\ln(r'/R_2) - \varepsilon^*\cos(\theta' - \omega t)] + \varepsilon^*[D_{pc} + 4\bar{V}V_c \ln(r'/R_2)]\cos \omega t$$
$$+ \varepsilon^*[D_{ps} + 4\bar{V}V_s \ln(r'/R_2)]\sin \omega t \qquad (16)$$

Closure Conditions

Equations (7), (12), (13), and (16) will describe the flow in the impeller and the volute after certain boundary conditions are satisfied. Even though β is referred to as the perturbation function, it was never assumed to be small. However, from the definition of the flow coefficient, β is required to have an average of one. The flow perturbation is further assumed to possess at least zeroth order continuity around the periphery of the impeller. This restriction on β can be met by satisfying the condition,

$$\beta(R_2,0) = \beta(R_2,2\pi) \qquad (17)$$

To account for what happens to the volute flow at the tongue, it is assumed that the average total head of the recirculated flow will be constant across the tongue, that is,

$$\int_{R_2'(0)}^{R_3'(0)} (P_v + \rho V_{\theta'}^2/2)\Big|_{\theta' = 2\pi} w\,dr' = \int_{R_2'(0)}^{R_3'(0)} (P_v + \rho V_{\theta'}^2/2)\Big|_{\theta' = 0} w\,dr' \qquad (18)$$

From the remaining flow that is discharged, the flow path angle, γ, will be determined. Previously it was stated that this angle will vary with flowrate and total head. Using this stipulation, γ can be found by equating the predicted and experimental total head rises across the pump. This requires that

$$\psi_{exp} = \bar{\psi} = [\overline{D_p}(2\pi) + C_v\bar{V}^2(2\pi)]/2 \qquad (19)$$

where

$$C_v = 1 + 2[\overline{\ln rA}(2\pi) - \overline{\ln rA}(0)]/[\bar{A}(2\pi) - \bar{A}(0)]$$

Admittedly, using an experimental result does limit the preliminary design applications of this model. However, the "H/Q" curve (in dimensionless form the function $\psi_{exp}(\phi)$) is normally available for any pump and it is important that this fundamental characteristic is properly represented in the model.

This completes the development of the equations necessary to obtain β, D_p, and V. The nine ordinary differential equations of (7), (12), and (13) were solved using centered differencing. The initial conditions of β, D_p, and V were chosen in an iterative manner to satisfy the closure conditions stated above.

Hydrodynamic Forces on the Impeller

Basically, there are two sources that contribute to the radial hydrodynamic forces on the impeller. One part is due to asymmetric pressure distribution around the impeller. The other is caused by the asymmetric momentum fluxes at the impeller inlet and discharge. The first contribution is evaluated by integrating the pressure around the inlet and discharge of the impeller:

$$\underset{\sim}{F}_p = (F_x + jF_y)_p = b\int_0^{2\pi} P_i(R_1,\theta_1)R_1 e^{j\theta_1} d\theta_1 - W_i\int_0^{2\pi} P_i(R_2,\theta_2)R_2 e^{j\theta_2} d\theta_2 \tag{20}$$

where j denotes the imaginary part that corresponds to the y direction (see Figure 2). The second contribution is found by applying the momentum equation to obtain

$$\begin{aligned}\frac{\underset{\sim}{F}_m}{\rho b} = \frac{(F_x + jF_y)_m}{\rho b} = &- e^{j\Omega t}\frac{\partial}{\partial t}\int_0^{2\pi}\int_{R_1}^{R_2}(v_r'' + jv_\theta'')e^{j\theta''}r''dr''d\theta'' \\ &- e^{j\Omega t}\Big[\int_0^{2\pi}(v_r'' + jv_\theta'')v_r''e^{j\theta''}r''d\theta''\Big]\Big|_{R_1}^{R_2} \\ &- e^{j\Omega t}2\Omega\int_0^{2\pi}\int_{R_1}^{R_2}(jv_r'' - v_\theta'')e^{j\theta''}r''dr''d\theta'' \\ &+ \omega^2\varepsilon\pi(R_2^2 - R_1^2)e^{j\omega t}\end{aligned} \tag{21}$$

When the pressure distributions of Equations (6) and (7) and the velocity profiles described by the no inlet pre-swirl condition and Equations (3)-(5) are applied to Equations (20) and (21), the resulting force on the impeller is

$$\underset{\sim}{F}^* = \underset{\sim}{F}_p^* + \underset{\sim}{F}_m^* = \bar{\underset{\sim}{F}} + \varepsilon^*(\underset{\sim}{F}_c \cos\omega t + \underset{\sim}{F}_s \sin\omega t) \tag{22}$$

where

$$\begin{aligned}\bar{\underset{\sim}{F}} = &\phi^2[W_i^*\sec^2\gamma + \underset{\sim}{k}R - 2 + 2j\tan\gamma]\int_0^{2\pi}\bar{\beta}^2(\theta_2)e^{j\theta_2}d\theta/2\pi \\ &- j\phi[W_i^*\sec^2\gamma\ln(R) + 1]\int_0^{2\pi}\bar{\beta}(\theta_2)e^{j\theta_2}d\theta_2/\pi\end{aligned} \tag{23a}$$

$$\begin{aligned}\underset{\sim}{F}_c = &\phi^2[W_i^*\sec^2\gamma + \underset{\sim}{k}R - 2 + 2j\tan\gamma]\int_0^{2\pi}\bar{\beta}(\theta_2)\beta_c(\theta_2)e^{j\theta_2}d\theta_2/\pi \\ &- j\phi[W_i^*\sec^2\gamma\ln(R) + 1]\int_0^{2\pi}\beta_c(\theta_2)e^{j\theta_2}d\theta_2/\pi \\ &+ \frac{\omega}{\Omega}\phi[W_i^*\sec^2\gamma\ln(R) + \underset{\sim}{k}/R - 1]\int_0^{2\pi}\beta_s(\theta_2)e^{j\theta_2}d\theta_2/\pi \\ &+ \frac{\omega}{\Omega}[\phi R W_i^*\int_0^{2\pi}\bar{\beta}(\theta_2)\sin(\theta_2 + \tan\gamma\ln(R))e^{j\theta_2}d\theta_2/\pi]\end{aligned}$$

$$- \frac{\omega}{\Omega}[2j\phi + W_i^*/(\underset{\sim}{k}\, R)] - \frac{\omega^2}{\Omega^2}\{W_i^*[1 - 1/(\underset{\sim}{k}\, R)]/\tan^2\gamma - 1 + 1/R^2\} \qquad (23b)$$

$$\begin{aligned} \underset{\sim}{F}_s = {} & \phi^2[W_i^*\sec^2\gamma + \underset{\sim}{k}\, R - 2 + 2j\tan\gamma]\int_0^{2\pi}\bar{\beta}(\theta_2)\beta_s(\theta_2)e^{j\theta_2}d\theta_2/\pi \\ & - j\phi[W_i^*\sec^2\gamma\ln(R) + 1]\int_0^{2\pi}\beta_s(\theta_2)e^{j\theta_2}d\theta_2/\pi \\ & - \frac{\omega}{\Omega}\,\phi[W_i^*\sec^2\gamma\ln(R) + \underset{\sim}{k}/R - 1]\int_0^{2\pi}\beta_c(\theta_2)e^{j\theta_2}d\theta_2/\pi \\ & - \frac{\omega}{\Omega}\,[\phi\, R\, W_i^*\int_0^{2\pi}\bar{\beta}(\theta_2)\cos(\theta_2 + \tan\gamma\ln(R))e^{j\theta_2}d\theta_2/\pi] \\ & - \frac{\omega}{\Omega}\, j[2j\phi + W_i^*/(\underset{\sim}{k}\, R)] - \frac{\omega^2}{\Omega^2}\, j\,\{W_i^*[1 - 1/(\underset{\sim}{k}\, R)]/\tan^2\gamma - 1 + 1/R^2\} \qquad (23c) \end{aligned}$$

and, $\underset{\sim}{k} = \cos(\tan\gamma\ln(R)) + j\sin(\tan\gamma\ln(R))$. Expressed in the terms used in Equation (1), these components are

$$\bar{\underset{\sim}{F}} = \bar{F}_x + j\bar{F}_y\ , \quad \underset{\sim}{F}_c = A_{xx}^* + jA_{yx}^*\ , \quad \text{and} \quad \underset{\sim}{F}_s = A_{xy}^* + jA_{yy}^* \qquad (24a\text{-}c)$$

Presentation of the calculated results will be postponed so that the experimental and theoretical results can be discussed together.

TEST FACILITY

The experimental results presented in this paper were obtained using the Rotor Force Test Facility at the California Institute of Technology, Pasadena. Details of the equipment have been given in previous papers [3,4,10], so only a brief description will be presented here. Figure 4 shows the test section where the centrifugal pump being examined is located. The impeller is mounted on the internal balance and the entire assembly is turned by the main shaft. The main shaft passes through an eccentrically drilled cylinder, which when rotated, causes the impeller to whirl in a 0.0990 inch diameter circular orbit. Forces on the impeller are sensed through strain gauges on four posts located in the internal balance. The relationships between the strains and forces were found by static calibration tests.

Descriptions of the impeller and one of the volutes that were tested are given in Figures 5 and 6. The impeller (referred to as Impeller X) is a five bladed cast bronze impeller with a specific speed of 0.57 and blade angle of 65°. The 86° spiral volute (Volute A) is constructed of fiberglass and designed to be "well matched" with Impeller X at a flow coefficient of 0.092. The dimensions of the volute cross-sections, shown in Figure 6, were used in evaluating the integrals of Equations (14a-e).

Two modifications have been made on the test facility for the benefit of this research. They were considered necessary in order isolate the interaction between the impeller and the volute from external influences. The modifications are illustrated in Figure 7. To separate the flow in the volute from the annular gap region, rings were installed 0.005 inch from the edge of the impeller. In addition, the flange of the test section was removed so that the front shroud of the impeller was exposed to the "reservoir-like" conditions of the test chamber (see Figure 4).

The removal of the front flange of the test section was judged to be essential after pressure measurements were made in the annual gap region with the flange in place and the rings removed. The measurements indicated that the fluid trapped in this region was responsible for a hydrodynamic stiffness (see Equation (26)) given approximately by

$$\begin{bmatrix} K_{xx} & K_{xy} \\ K_{yx} & K_{yy} \end{bmatrix} = \begin{bmatrix} -1.6 & 0.3 \\ -0.3 & -1.6 \end{bmatrix}$$

When compared with Chamieh's [5] direct measurements of the total hydrodynamic stiffness on the impeller (annular gap plus volute) given approximately by

$$\begin{bmatrix} K_{xx} & K_{xy} \\ K_{yx} & k_{yy} \end{bmatrix} = \begin{bmatrix} -2.0 & 0.9 \\ -0.9 & -2.0 \end{bmatrix}$$

it is seen that the contribution from the annular gap is significant. With the flange removed, it was anticipated that the fluid forces on the front shroud of the impeller would be largely eliminated.

COMPARISONS BETWEEN EXPERIMENTAL AND THEORETICAL RESULTS

A preliminary step in the theoretical calculations must be the estimation of the impeller flow path angle, γ (see Section 2(a)). In practice, information on the actual total head rise as a function of flowrate is almost always available; an example for Impeller X and Volute A is presented in Fig.8. By setting $\bar{\psi}=\psi_{exp}$, the flow path angle, γ, shown in Fig.9 was obtained. Note that the typical magnitude of γ is about 80° while the blade angle of Impeller X is 65°.

Measurements of the static pressure of the discharge from the impeller were made using holes drilled at the inlet to the volute (see Figures 6 and 7). The circumferential pressure distributions are compared with the theoretical results in Figures 10 and 11. The pressure taps were alternately placed in the front and back of the volute, resulting in the slight oscillation of the data. The results were obtained for a range of shaft speeds from $\Omega = 800$ to 1200 RPM, but the non-dimensionalized pressures were found to be independent of the speed. Figure 10 shows that the theory gives a good approximation of the the pressure distributions over a moderate range of flow coefficients. For flow coefficients larger than this range, the correlation begins to falter as shown in Figure 11. It was concluded that the deviation was caused by the inadequacy of a one dimensional treatment of the flow near the tongue of the volute. At the higher flowrates, it has been suggested [11] that there is a reversal of the direction of flow in the region just inside the tongue. The effect on the pressure distribution of displacing the impeller is also demonstrated in Figure 11. The model appears to follow the changes that occur, even when the absolute pressure predictions are rather poor.

A comparison between the experimental and theoretical steady forces on the impeller is given in Figure 12. One set of experimental results was obtained by placing the impeller in four equally spaced orbit positions and then averaging the internal balance force measurements. The second set (for $\phi = 0.06$ and 0.10) was obtained by integration of the discharge pressure measurements. The theoretical model tends to overpredict the steady or average radial forces somewhat, but it does give reasonable results considering the crudeness of the model. Colding-Jorgensen's [6] steady force calculations for a 67.5° blade angle impeller in an 86° spiral volute are also shown in Figure 12. The present model appears to give a more accurate assessment of the steady forces when compared with the experimental results. The agreement between the two sets of experimental data indicates that the primary cause of the radial force is the asymmetric pressure distribution at the discharge of the impeller. Moreover, the theoretical model predicted that the discharge pressure was responsible for 99% of the total force on the impeller while the net momentum flux contribution was essentially negligible. It might also be of interest to note that over the entire range of flowrates for which theoretical results are presented, the predicted perturbation in the impeller discharge flow never exceeded 6% of the mean flow.

Figure 13 presents the components of the generalized hydrodynamic force matrix, [A], that result when the impeller whirls in an eccentric orbit at the pump design flowrate ($\phi = 0.092$). From the experimental data, it is seen that the cross-coupled terms (i.e. A_{xy}, A_{yx}) imply that forces act in the direction of the whirl orbit up to $\omega/\Omega = 0.10$. This destabilizing influence is predicted by the theoretical model to occur up to $\omega/\Omega = 0.14$. Due to the coupled nature of Equations (7b) and (7c), it was not possible to calculate [A] beyond the range of whirl ratios shown in Figure 13. This problem is believed to be the result of the current limitations of the iterative technique used in obtaining the solution.

As was mentioned in the introduction, it is a standard practice to express the matrix elements of [A] in powers of ω. By examining the A_{yx} term in Figure 13, it is apparent that a quadratic in ω will not adequately describe the features of the matrix element. A cubic, however, can approximate all of the [A] matrix element variations with ω giving the coefficients of such an expansion as

$$\begin{bmatrix} A_{xx} & A_{xy} \\ A_{yx} & A_{yy} \end{bmatrix} = \begin{bmatrix} -K_{xx} - \omega C_{xy} + \omega^2 M_{xx} + \omega^3 J_{xy} & -K_{xy} + \omega C_{xx} + \omega^2 M_{xy} - \omega^3 J_{xx} \\ -K_{yx} - \omega C_{yy} + \omega^2 M_{yx} + \omega^3 J_{yy} & -K_{yy} + \omega C_{yx} + \omega^2 M_{yy} - \omega^3 J_{yx} \end{bmatrix} \tag{25}$$

or alternatively as

$$[A(\omega/\Omega)] \begin{Bmatrix} x \\ y \end{Bmatrix} = -[K] \begin{Bmatrix} x \\ y \end{Bmatrix} - [C] \begin{Bmatrix} \dot{x} \\ \dot{y} \end{Bmatrix} - [M] \begin{Bmatrix} \ddot{x} \\ \ddot{y} \end{Bmatrix} - [J] \begin{Bmatrix} \dddot{x} \\ \dddot{y} \end{Bmatrix} \tag{26}$$

where

$$x = \varepsilon \cos \omega t \text{ and } y = \varepsilon \sin \omega t$$

The [K], [C], and [M] matrices correspond to the stiffness, damping, and inertial components that are commonly employed in rotordynamics. Since the [J] matrix is related to the third order time derivative of the impeller displacement (which is conventionally known as the jerk), it will be referred to as the "jerk" matrix.

The resulting [K] matrix elements of the cubic expansion are given in Figure 14, and the [C], [M], and [J] matrix elements are presented in Figure 15. Included in Figure 14 are the stiffnesses that were calculated using the force measurements (from the internal balance and the pressure distributions) taken at four impeller positions. Also shown in Figure 14 are the stiffnesses predicted by Colding-Jorgensen [6] for an 86° spiral volute. With the exception of the K_{yx} term, the current model does a fair job of describing the variation of stiffness with flowrate. The magnitudes, however, tend to be underpredicted by the theory. Over most of the range of flow coefficients, the stiffness is such that it would encourage the whirling motion of the impeller. The same is also true of the damping when the flowrate drops below $\phi = 0.07$ as shown in Figure 15. The magnitude of the damping components computed by [6] (not shown here) were less than 10% of those predicted by the present model. In general, the inertial force would discourage an orbital motion of the impeller, but it will tend to drive the impeller in the direction of the displacement. The jerk force attains significant values only at the lower flow coefficients.

CLOSING COMMENTS

A theoretical model has been developed to describe the flow in the impeller and the volute, along with the interactions that occur between them. This investigation was undertaken to provide a better understanding of the destabilizing hydrodynamic forces that have been observed [5,10] on a whirling centrifugal pump impeller. To implement the model requires only a knowledge of the dimensions of the volute and impeller, and the total head rise across the entire pump. Comparisons between the predicted and experimental results are encouraging. Experimentation with different volute geometries and over a wider range of operating conditions (flow coefficient and whirl ratio) would provide a more crucial test of the theoretical model. It might also prove insightfull to incorporate the effects of inducers and diffuser vanes into the theoretical model. These devices are now commonly employed on many high performance centrifugal pumps.

Previous experimental results [5,10] have tended to over-estimate the contribution of the volute/impeller interaction to the total stiffness force acting on the impeller. The over-estimation came about because of an asymmetric pressure distribution in the fluid trapped on the front shroud of the impeller. Since real pumps do have fluid in this region, it will be important in the future to perform a detailed study of this area.

ACKNOWLEDGEMENTS

This research was funded by NASA George Marshal Space Flight Center, Huntsville, Alabama under contract NAS 8-33108. Both of the authors would like to express their gratitude to A.J. Acosta and T.K. Caughey for their helpful advice, and R. Franz and N. Ardnt for their assistance with the experiments. One of the authors (D.R. Adkins) would also like to thank the Shell Companies Foundation for a fellowship that supported his graduate studies and Susan Berkley for her invaluable help in preparing this paper.

REFERENCES

1. Adkins, D.R., "Analyses of Hydrodynamic Forces on Centrifugal Pump Impellers", Ph.D. Thesis, Division of Engineering and Applied Sciences, California Institute of Technology, 1985.

2. Agostinelli, A., Nobles, D., and Mockridge, C.R., "An Experimental Investigation of Radial Thrust in Centrifugal Pumps", Trans. ASME, J. of Engr. for Power, Vol. 82, pp. 120-126, April 1960.

3. Brennen, C.E., Acosta, A.J., and Caughey, T.K., "A Test Program to Measure Fluid Mechanical Whirl-Excitation Forces in Centrifugal Pumps", First Workshop on Rotordynamic Instability Problems in High Performance Turbomachinery, Texas A&M University, NASA Conf. Pub. 2133, pp. 229-235, 1980.

4. Chamieh, D.S., "Forces On A Whirling Centrifugal Pump-Impeller", Ph.D. Thesis, Division of Engineering and Applied Sciences, California Institute of Technology, 1983.

5. Chamieh, D.S., Acosta, A.J., Brennen, C.E., Caughey, T.K., and Franz, R., "Experimental Measurements of Hydrodynamic Stiffness Matrices for a Centrifugal Pump Impeller", 2nd Workshop on Rotordynamic Instability Problems in High Performance Turbomachinery, Texas A&M University, NASA Conf. Pub. 2250, pp. 382-398, May 10-12, 1982.

6. Colding-Jorgensen, J., "The Effect of Fluid Forces on Rotor Stability of Centrifugal Compressors and Pumps", First Workshop on Rotordynamic Instability Problems in High Performance Turbomachinery, Texas A&M University, NASA Conf. Pub. 2133, pp. 249- 266, May 12-14, 1980.

7. Csanady, G.T., "Radial Forces in a Pump Caused by Volute Casing", Trans. ASME, J. of Engr. for Power, Vol. 84, pp. 337-340, October 1962.

8. Ehrich, F., and Childs, D., "Self-Excited Vibration in High Performance Turbomachinery", Mech. Engr., Vol. 106, No. 5, pp. 66-79, May 1984.

9. Iversen, H.W., Rolling, R.E., and Carlson, J.J., "Volute Pressure Distribution, Radial Force on the Impeller and Volute Mixing Losses of a Radial Flow Centrifugal Pump", Trans. ASME, J. of Engr. for Power, Vol. 82, pp. 136-144, April 1960.

10. Jery, B., Acosta, A.J., Brennen, C.E., and Caughey, T.K., "Hydrodynamic Impeller Stiffness, Damping and Inertia in the Rotordynamics of Centrifugal Flow Pumps", Rotordynamic Instability Problems in High Performance Turbomachinery, Texas A&M University, NASA Conf. Pub. 2338, pp. 137-160, May 28-30, 1984.

11. Lazarkiewicz, S., and Troskolanski, A.T., "Impeller Pumps", Pergamon Press, Translated by D.K. Rutter (Polish Ed. Title: Pompy Wirowe), 1965.

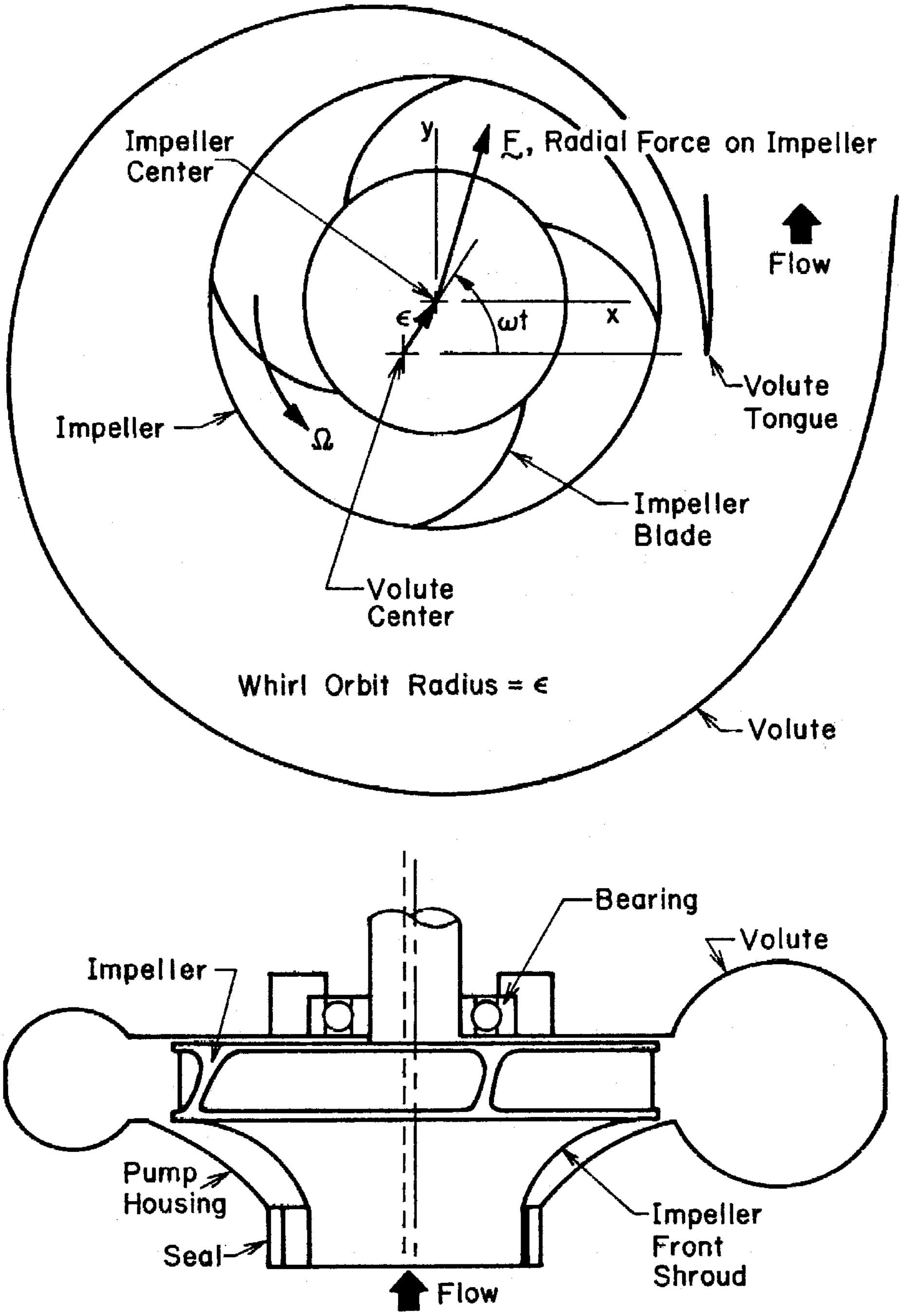

Figure 1. Description of a centrifugal pump.

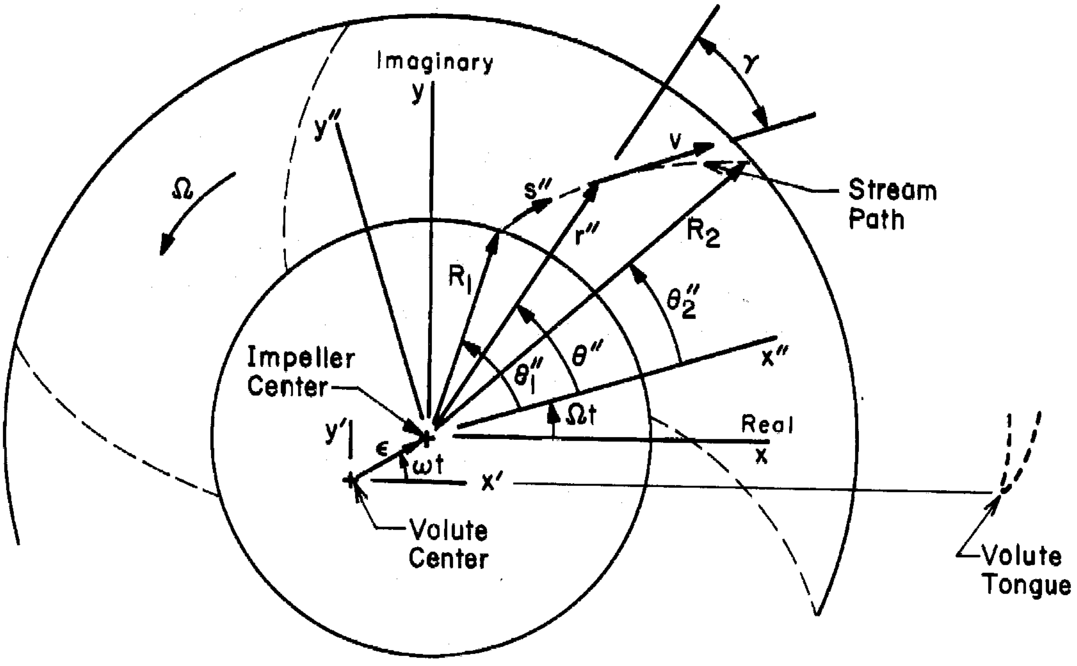

Figure 2. Geometry of a centrifugal pump impeller.

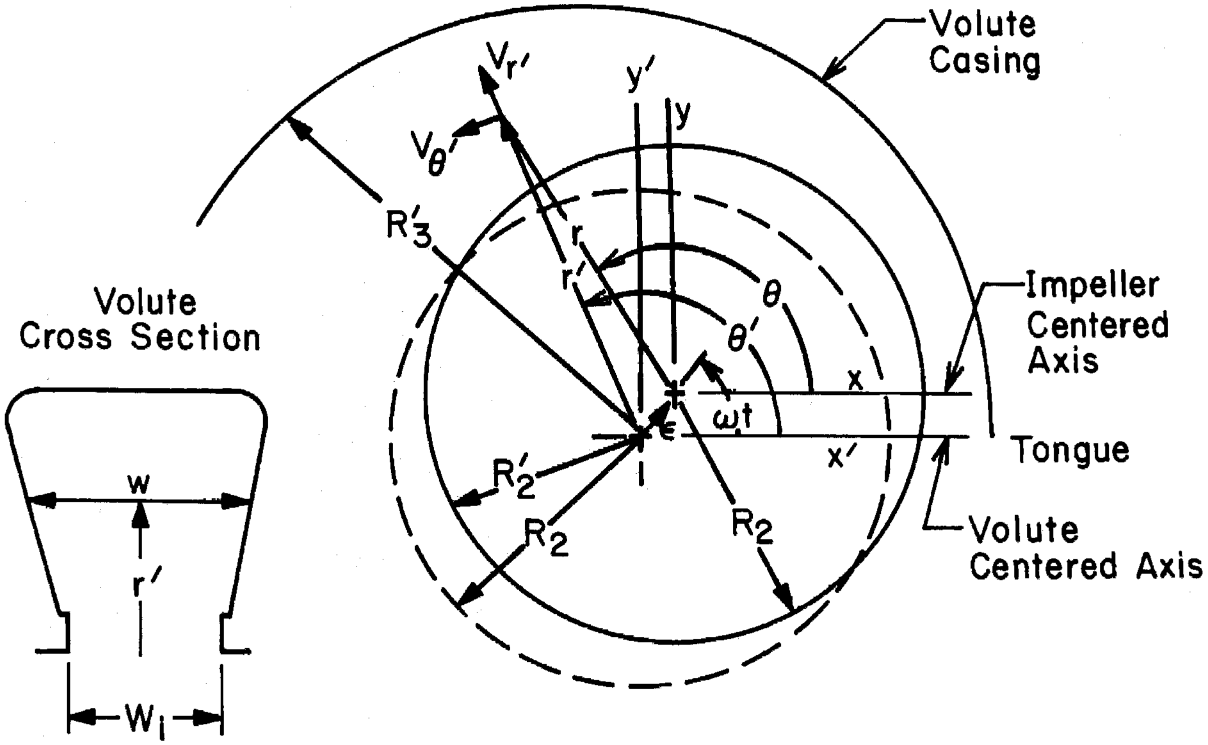

Figure 3. Geometry of a volute.

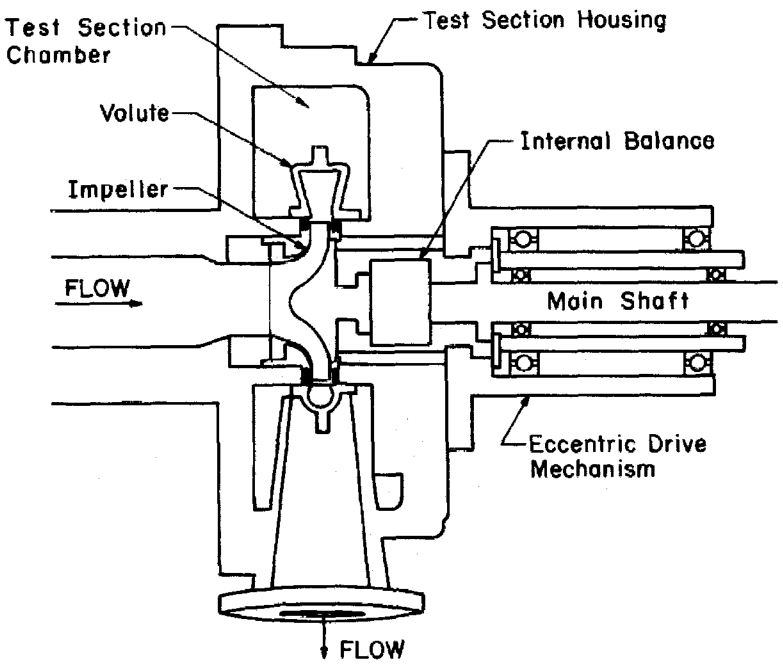

Figure 4. Schematic of the test section.

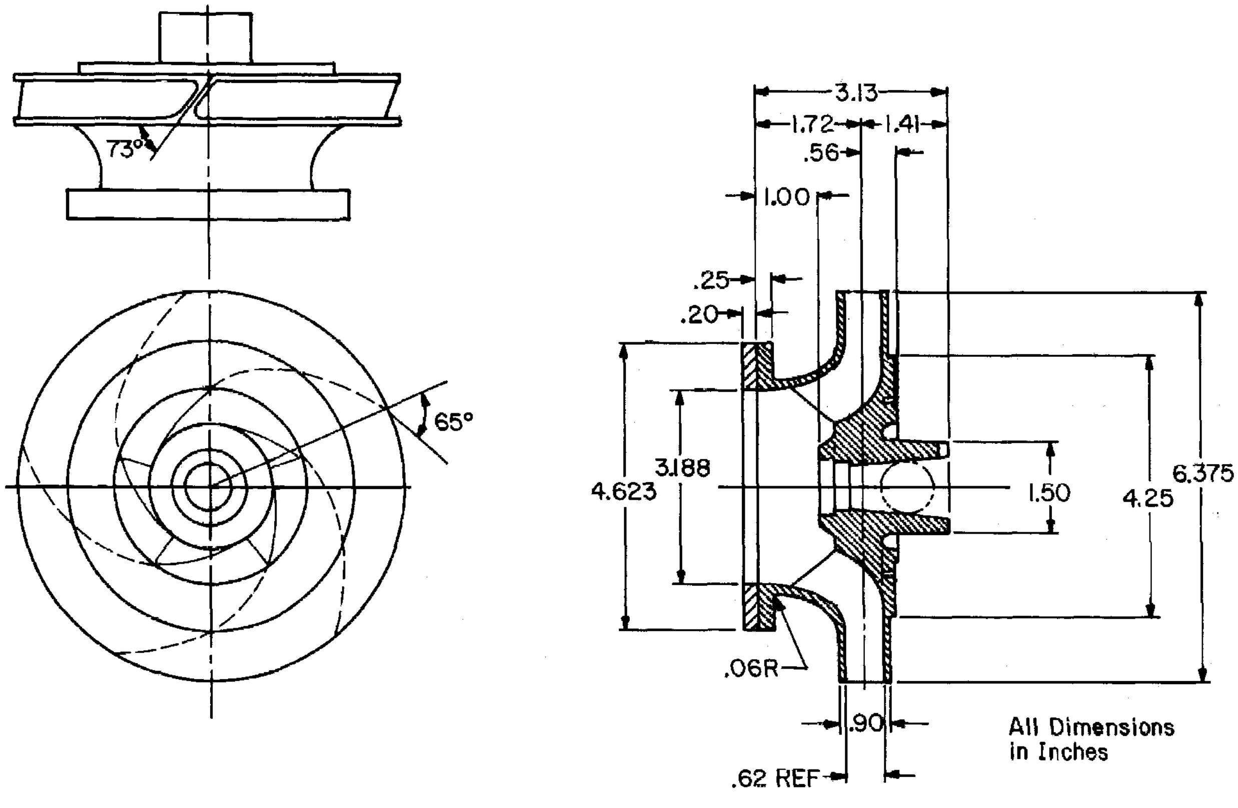

Figure 5. Dimensions of Impeller X.

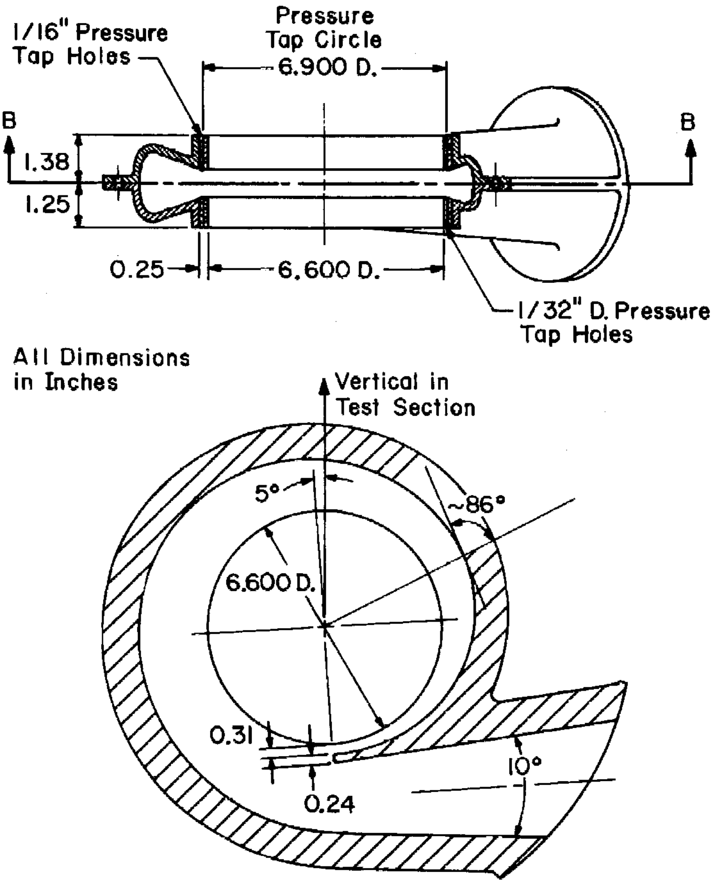

Section B-B

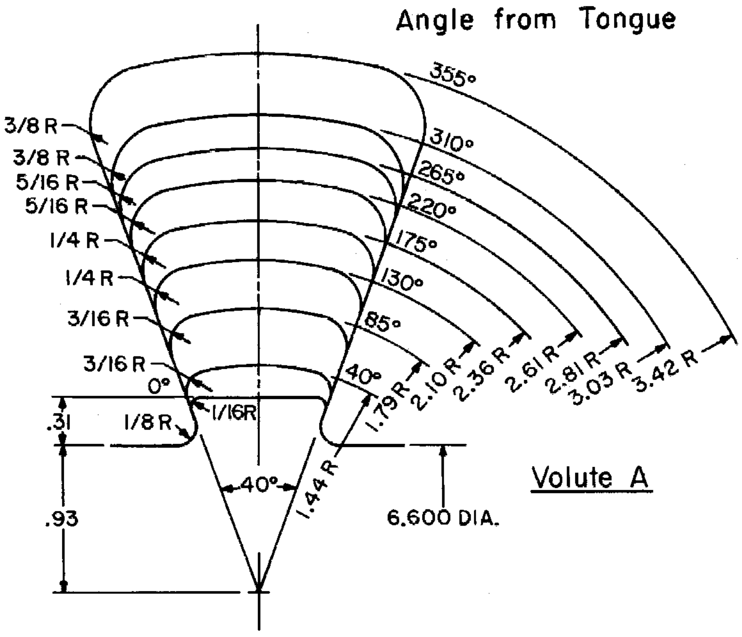

Figure 6. Dimensions of Volute A.

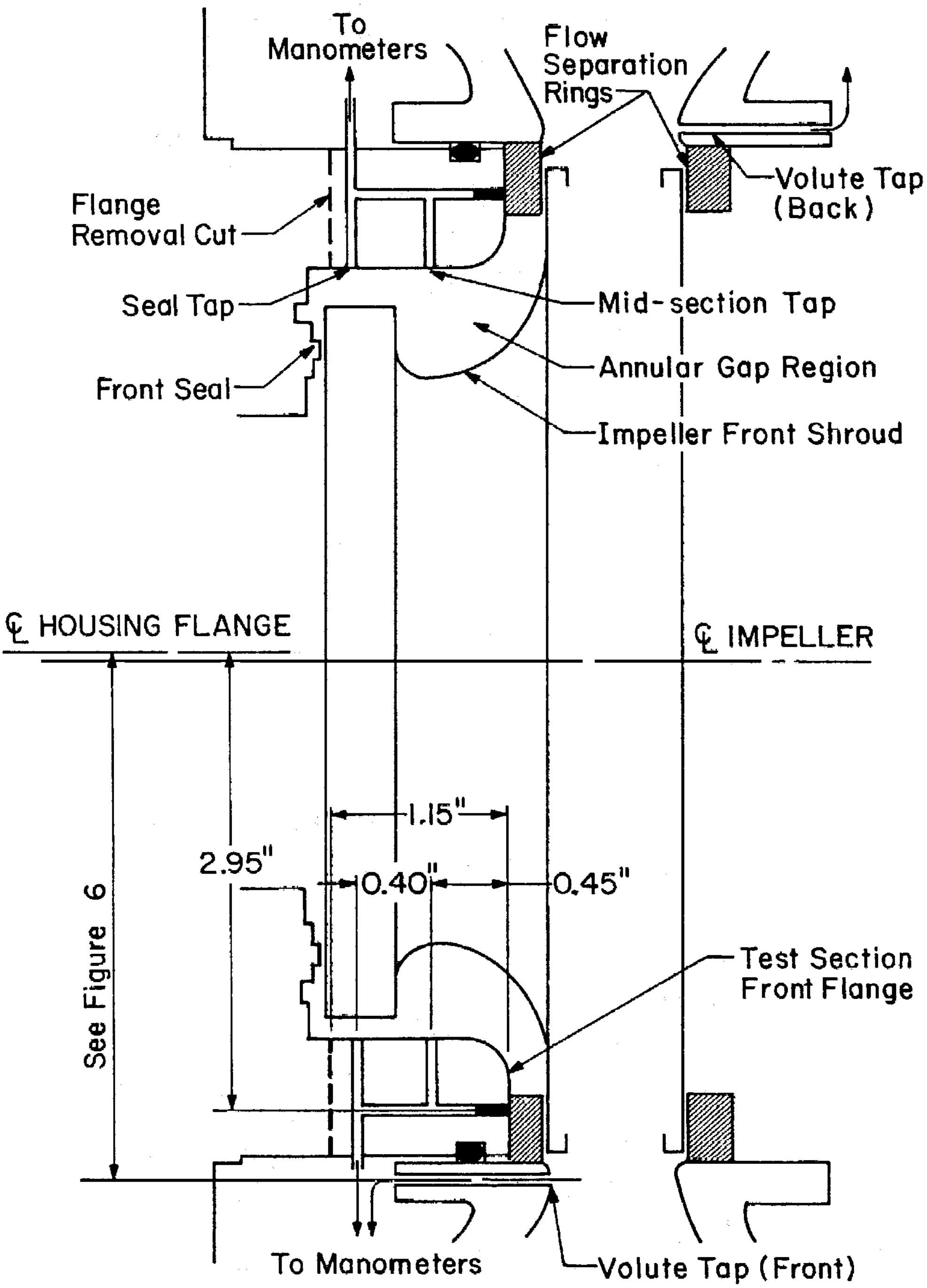

Figure 7. Modifications of the test facility.

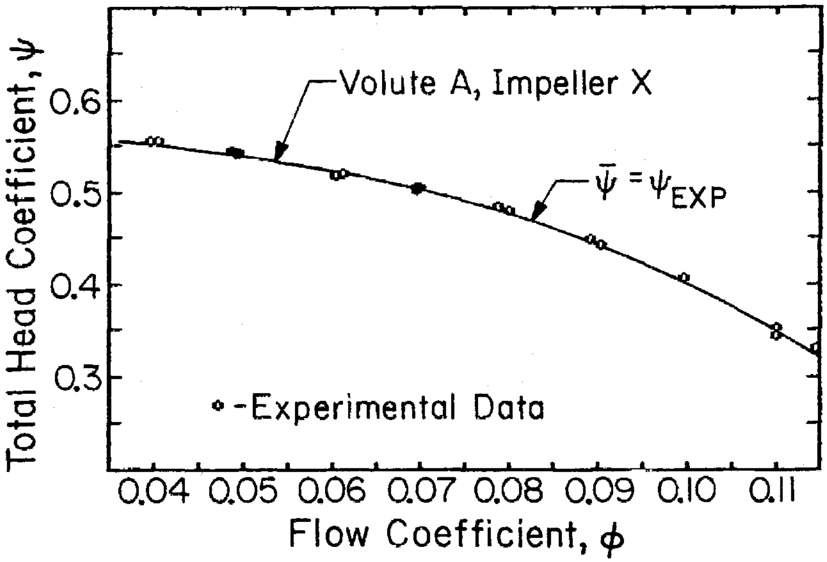

Figure 8. Total head coefficient vs. the flow coefficient for the Impeller X and Volute A pump. The solid line represents the average value of the experimental data.

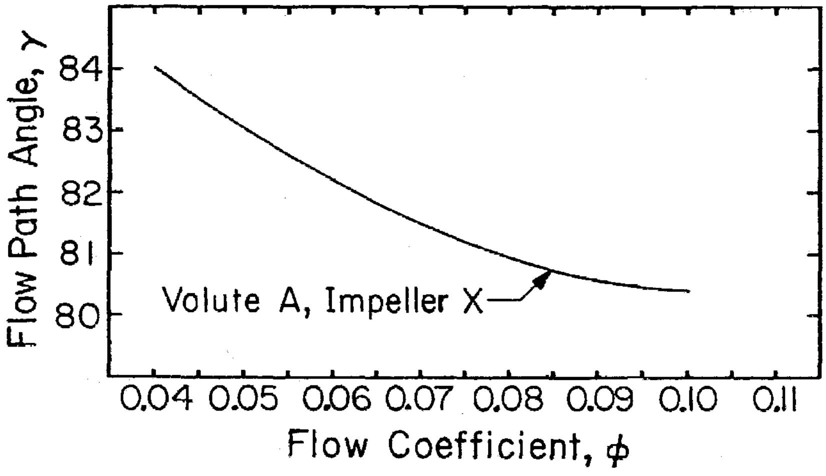

Figure 9. The average angle the flow follows through the pump (measured with respect to the radial line) as a function of flowrate.

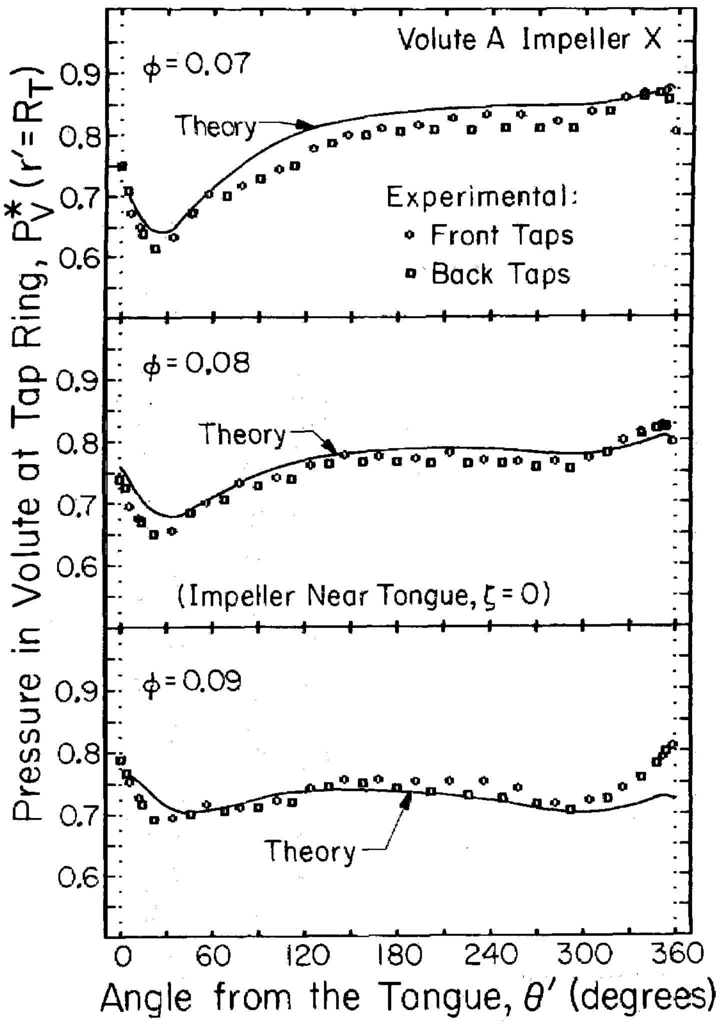

Figure 10. Experimental and theoretical pressure distributions at the inlet of the volute for three different flowrates with the impeller placed near the tongue. Measurements were taken with $\Omega = 1000$ RPM.

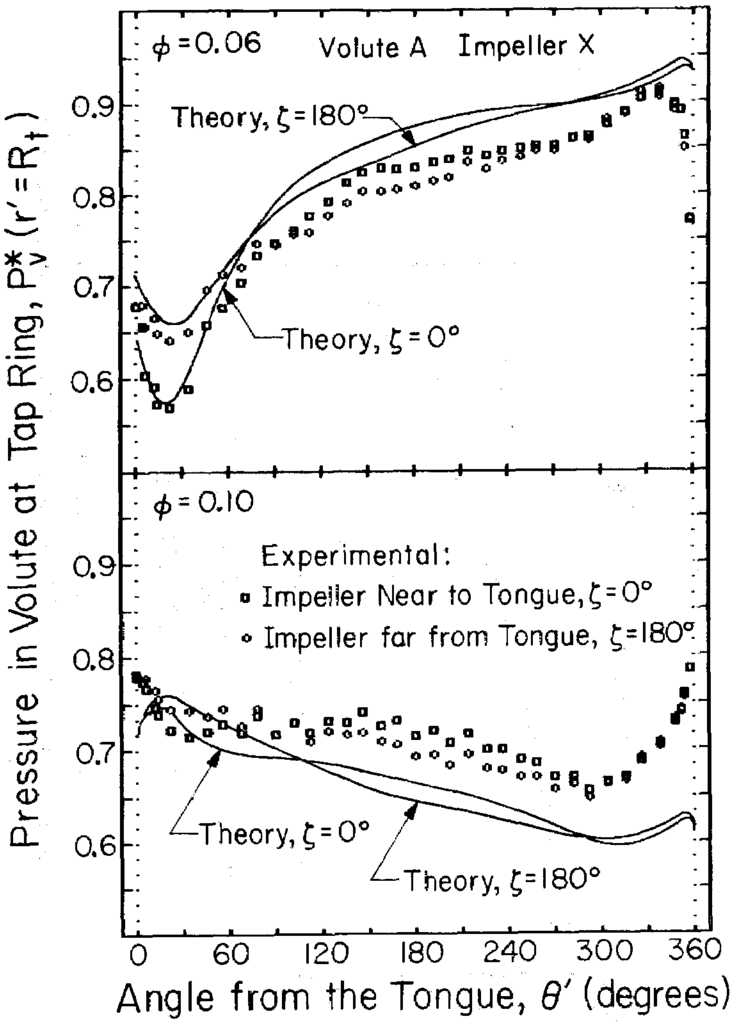

Figure 11. Experimental and theoretical pressure distributions at the inlet of the volute for two different flowrates with the impeller placed near to and far from the volute tongue.

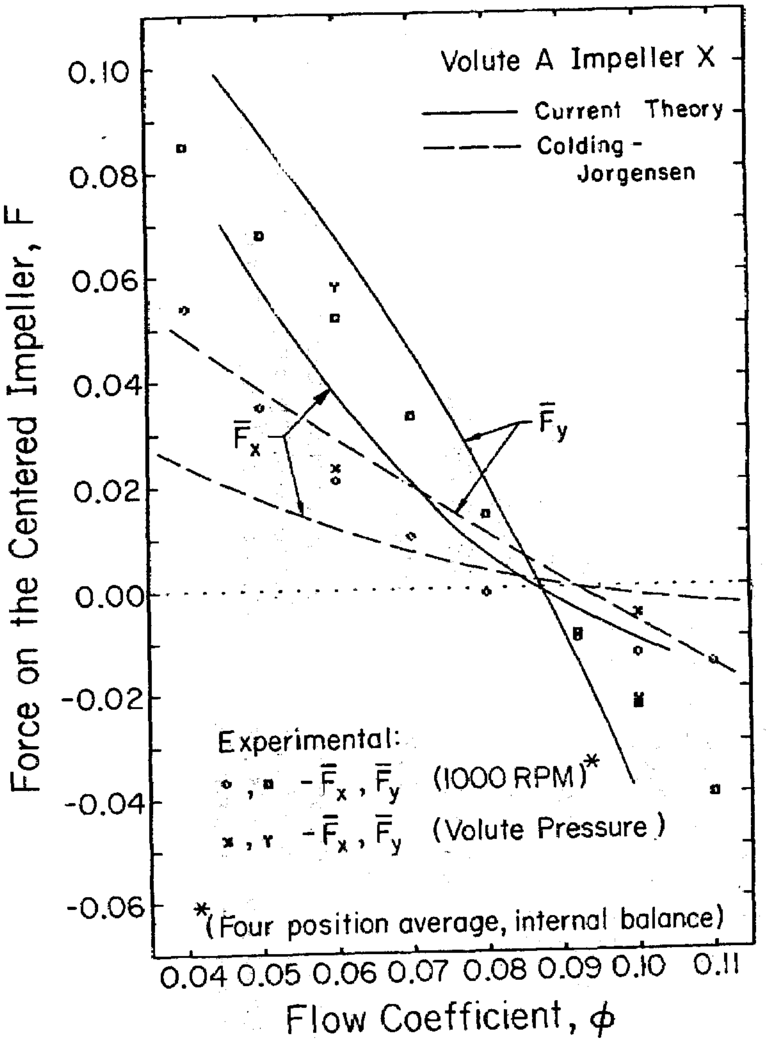

Figure 12. Steady hydrodynamic forces acting upon Impeller X as function of flowrate. Experimental forces were obtained by both internal balance and discharge pressure measurements. Colding-Jorgensen's [6] results are for an 86° spiral volute with a 67.5° blade angle impeller.

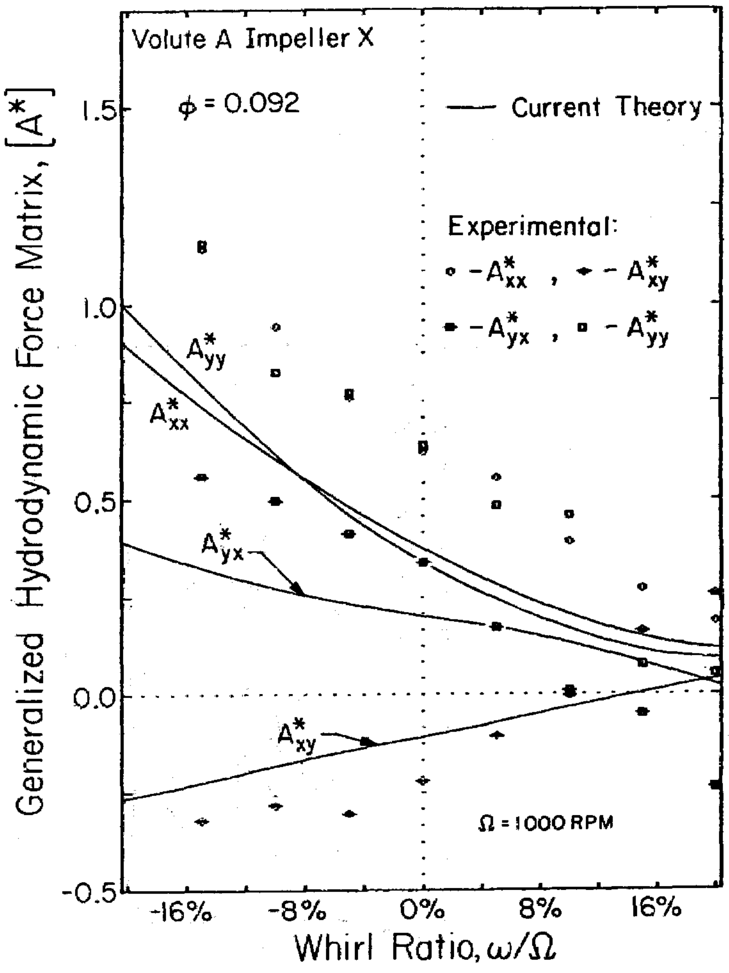

Figure 13. The Generalized Hydrodynamic Force coefficients as functions of whirl speed at the volute design flow coefficient ($\phi = 0.092$). The experimental results were obtained from the direct force measurements of the internal balance. The radius of the whirl orbit for Impeller X was $\epsilon = 0.0495$ inches.

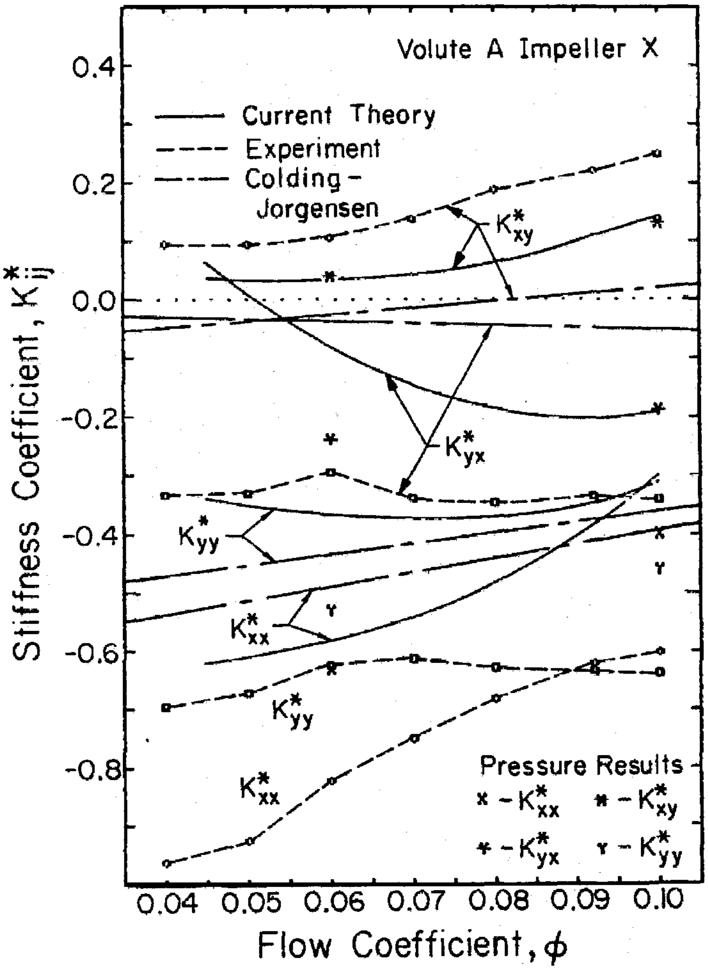

Figure 14. Hydrodynamic stiffnesses as functions of the flowrate. Experimental results are from internal balance and pressure measurements. Colding-Jorgensen's [6] results are for an 86° spiral volute with a 67.5° blade angle impeller.

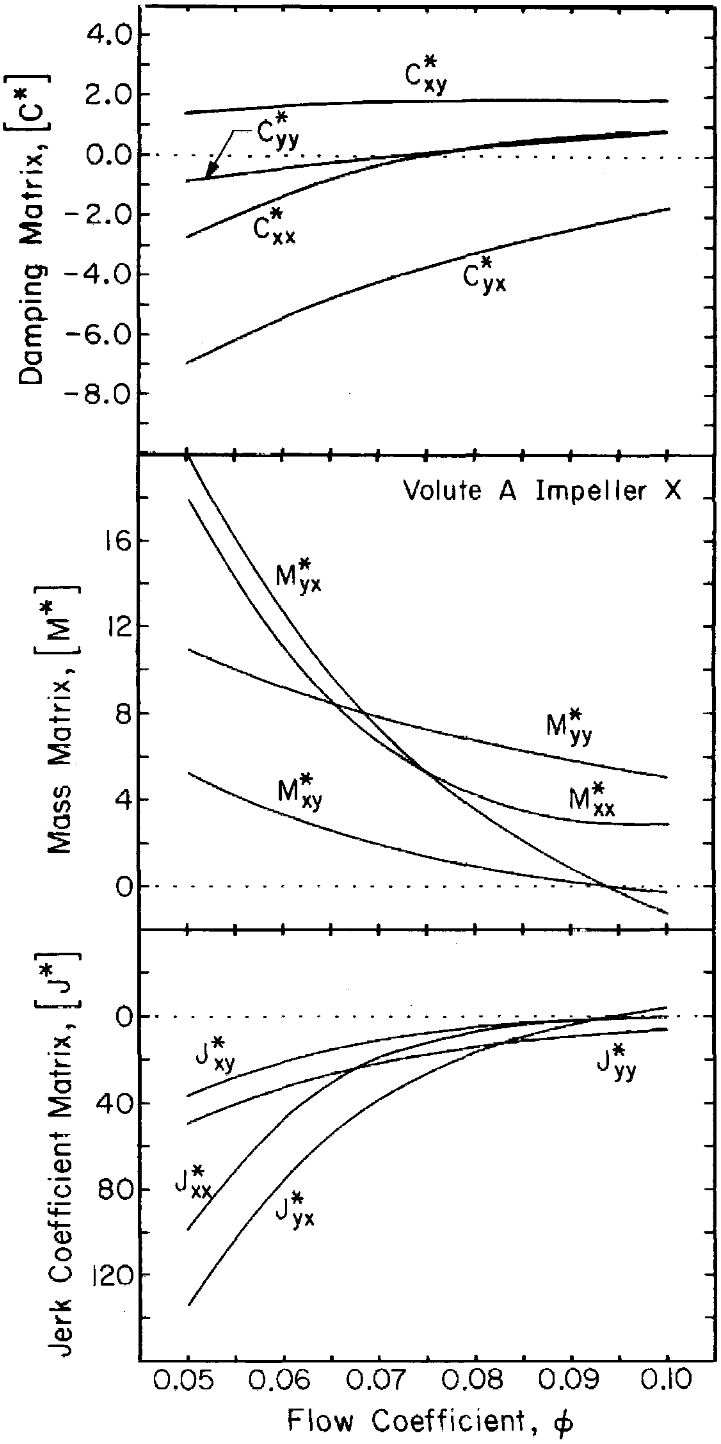

Figure 15. Damping, mass, and jerk force coefficients as functions of the flowrate as predicted by the current theoretical model.